Available online at www.sciencedirect.com
ScienceDirect
Polymer 47 (2006) 8562–8574
polymer
www.elsevier.com/locate/polymer

Plastic deformation behavior of β-phase isotactic polypropylene in plane-strain compression at room temperature

E. Lezak, Z. Bartczak*, A. Galeski

Centre of Molecular and Macromolecular Studies, Polish Academy of Sciences, Polymer Physics, Sienkiewicza 112, 90-363 Lodz, Poland

Received 10 May 2006; received in revised form 5 October 2006; accepted 6 October 2006
Available online 13 November 2006

Abstract

Isotactic polypropylene (iPP) rich in β crystal modification (constituting 92% of crystalline phase) was deformed by the plane-strain compression with constant true strain rate, at room temperature. The evolution of phase structure, morphology and orientation was studied by DSC, X-ray and SEM.

The deformation sequence and the active deformation mechanisms were found out. The most important mechanisms were interlamellar slip operating in the amorphous layers, resulting in numerous fine deformation bands due to localization of deformation and the crystallographic slip systems, including the (110)[001] chain slip and (110)[$1\bar{1}0$] transverse slip.

Shear within deformation bands leads to β → smectic and β → α solid state phase transformations. At room temperature the β → smectic transformation appeared to be the primary transformation, yielding the oriented smectic phase with high concentration of 19 wt.% at the true strain of $e = 1.49$. The β → α yields only about 4 wt.% of new α-phase at the same strain. As a result of the deformation and phase transformation within numerous fine deformation bands β-lamellae are locally destroyed and fragmented into smaller crystals.

Another deformation mechanism is the cooperative kinking of lamellae, leading to their reorientation and formation of a chevron-like lamellar arrangement.

At high strains, above $e = 1$, an advanced crystallographic slip and high stretch of amorphous material due to interlamellar shear bring further heavy fragmentation of lamellar crystals, earlier fragmented partially by deformation bands. This fragmentation is followed by fast rotation of small unconstrained crystallites with chain axis towards the direction of flow, FD. This process leads to development of the final texture of the highly deformed β-iPP with molecular axis of both crystalline and smectic phases oriented along FD.

Keywords: Isotactic polypropylene; Beta phase; Plastic deformation

1. Introduction

Isotactic polypropylene (iPP) is a polymorphic material which can crystallize in three crystalline forms, depicted as α (monoclinic), β (trigonal) and γ (orthorombic). At certain conditions, e.g. under high undercooling, a mesophase usually called 'smectic' is formed instead of crystalline phase. The iPP chains in the lattices of all three crystalline forms are 3_1 helices with either right or left handedness.

The most common crystal modification, formed at typical processing conditions, is the monoclinic α-form [1]. This structure with lattice parameters $a = 6.65$ Å, $b = 20.96$ Å, $c = 6.50$ Å, $\beta = 99.8°$ is characterized by a change in helical handedness of chains and azimuth orientation of chains on successive (040) planes. Lamellae of α-iPP reveal branching of crystallographic origin at the angle of approx. 80°, which is a unique feature in polymer crystallography. Such branching leads to the formation of two populations of lamellae of radial (mother) and tangential (daughter) orientations in spherulitic growth [2,3] and results in the so-called 'cross-hatched' lamellar morphology within spherulites. Many experimental observations demonstrated that α-modification is thermodynamically the most stable crystalline form of iPP [1].

Another crystalline form of iPP is the β-modification [4]. Crystals of this form, thermodynamically less stable than

* Corresponding author. Tel.: +48 42 680 3237; fax: +48 42 684 7126.
E-mail address: bartczak@bilbo.cbmm.lodz.pl (Z. Bartczak).

0032-3861/$ - see front matter © 2006 Elsevier Ltd. All rights reserved.
doi:10.1016/j.polymer.2006.10.016

α [5], can be obtained only under specific conditions: either in the presence of specific nucleants [6–10] or by special modification of crystallization conditions, e.g. crystallization in the presence of shear [11–13] or temperature gradient [14]. The crystal structure of β-modification of iPP was established independently by Meille et al. [15] and Lotz et al. [16] as trigonal with unit cell parameters $a = b = 11.01$ Å, $c = 6.5$ Å, $\alpha = \beta = 90°$ and $\gamma = 60°$, containing three isochiral 3_1 helices, which is in contrast to the alternating helical handedness found in α crystal form. Isochiral helices forming the unit cell show different azimuth orientations: the chain in the corner of the unit cell is rotated by approx. 180° with respect to the two other chains located inside the cell. Growth of β-form lamellae usually results in spherulitic morphology, similarly to the α-form. However, the arrangement of lamellae in β-spherulites is solely radial, and there is no 'cross-hatched' morphology, typical for α-spherulites. This results in the formation of well individualized negatively birefringent spherulites, which can be easily distinguished from α-spherulites.

It was found that iPP rich in β-phase shows very interesting mechanical properties, in many aspects advantageous over conventional α-iPP, e.g. the impact strength, toughness or stress-whitening under tensile deformation of β-iPP markedly exceed those of α-iPP [5,10,17,18]. The improved mechanical performance of β-iPP as compared to α-iPP makes this polymer very attractive for numerous applications. Because of this the mechanical response, deformation behavior and associated structure evolution of iPP of both α- and β-modification, have been a subject of numerous recent studies.

Texture evolution of α-iPP and related deformation mechanisms was studied in uniaxial [19,20] and plane-strain compression [21] modes. Deformation mechanisms of crystallographic origin were found to be responsible for alignment of the *c* axis normal to the load direction in both deformation modes. The main active mechanisms found were the crystallographic slips along the chain direction: (010)[001], (110)[001] and (100)[001], supported by the deformation of the amorphous component by interlamellar slip [21]. High-rate deformation at room temperature also induced α → smectic phase transformation.

The deformation-induced texture of β-form has not been reported yet. Deformation of β-iPP was studied mostly in tensile experiments, where β-form appeared unstable, transforming readily either to the α-form [22–24] or to the mesophase [22,25]. The β → α transformation was considered as the main source for an improved toughness of β-iPP [24]. Solid-to-solid martensitic-like transformation and partial melting–recrystallization processes have been proposed to describe the β → α phase transformation. For long time the postulated β → α martensitic transformation seemed problematic since it would require reversal of helical handedness, which was considered impossible in solid [24]. Recently, Xu et al. [26] demonstrated, however, that β → α transformation in iPP is indeed the result of solid-to-solid phase transformation, which can be accomplished by a simultaneous solid transformation that contains a process of transverse partial slip along (110) or (120) plane of β crystal lattice and a shear of that lattice, all in the presence of conformational defects. The propagation of these conformational defects along chains provides the reversal of helical handedness required by the solid β → α transformation.

In addition to β → α and β → smectic phase transformations the activity of crystallographic chain and transverse slip systems (110)[001] and (110)[1$\bar{1}$0], both operating in the (110) plane, was postulated to be active during rolling of β-iPP [27].

The goal of the present study was to investigate the plastic deformation behavior and related evolution of the crystalline texture and lamellar orientation of iPP samples containing crystals of primarily β-form. On this basis we intended to identify active deformation mechanisms characteristic for this crystal modification and evaluate their role in the deformation process. Samples rich in β-form crystals were produced by crystallization in the presence of a specific nucleant. The plane-strain compression was chosen as the deformation mode for this study. Plane-strain compression, while kinematically similar to tensile drawing and leading to plastic flow in the direction perpendicular to compressive load, has several advantages over other modes of deformation, especially the most frequently used tensile mode. The two most important are (i) the deformation process is macroscopically homogeneous in the entire strain range, with no instabilities like neck usually observed in tension and (ii) deformation is virtually cavity-free, since the compressive stress component prevents notable cavitation, while single accidental cavities are quickly healed by advancing compression. During plane-strain compression the real mechanisms involved are not obscured by any unwanted side effects, and moreover, the progress of deformation can be studied effectively in a wide range of the strain. Furthermore, the true stress–true strain curves, characterizing deformation process, can be obtained in plane-strain compression easily. It should be also mentioned that constraints imposed on a sample in the plane-strain compression eliminate most of the problems which could be encountered in uniaxial compression (which is also a cavity-free mode), as those related to sample barreling or radial cracking at high strains.

2. Experimental

2.1. Materials and sample preparation

The material used in this investigation was a commercial-grade isotactic polypropylene homopolymer, Malen P, F-401 ($M_w = 297\,200$, $M_n = 56\,400$, melt flow index MFI (190 °C/2.16 kg) = 3 g/10 min, isotacticity index > 95%), provided by Basell Orlen Polyolefins (Poland). The polymer was stabilized against oxidation and thermal degradation.

The calcium salt of pimelic acid was used as a specific β-nucleating agent. It was synthesized from pimelic acid (Sigma–Aldrich) [28]. Powdered nucleant (0.2 wt.%) was mixed with molten iPP resin in the Plasticorder mixer (Brabender) at 200 °C.

Samples for deformation experiments, in the form of $60 \times 60 \times 4.5\ mm^3$ plates, were prepared by compression molding at 190 °C and pressure of 5 MPa. The molded plates were solidified by rapid cooling in a bath of ice water. All samples were crystallized at identical conditions to avoid any differences of supermolecular structure among them. Specimens of the size desired for particular experiment were machined out from these plates.

2.2. Plane-strain compression

The plane-strain compression tests were performed using a loading frame (Instron, Model 5582) and a compression tool, equipped with a load and strain gauges. This tool was a deep channel-die [29,30] with the channel 3.85 mm wide (i.e. along constrained direction, CD), 50 mm long (flow direction, FD), and 60 mm deep (loading direction, LD), allowing samples up to 50 mm high to be compressed. Specimens and the die were lubricated to reduce friction. Other details are given in Ref. [29].

Specimens of α- and β-iPP of the size $3.85 \times 50 \times 40$ mm (along CD, FD and LD, respectively) were deformed with a constant true strain rate of $0.05\ min^{-1}$, at room temperature up to the point of fracture. Additionally, a set of samples deformed to the desired intermediate true strains were prepared by deformation at the same conditions.

2.3. Characterization

2.3.1. DSC

Thermal analysis was carried out with a DSC apparatus (TA 2920, Thermal Analysis). The overall crystallinity was estimated on the basis of the heat of melting recorded during heating with the rate of 10 °C/min. The heat of melting of 100% crystalline α- and β-iPP of $\Delta h_f(\alpha) = 177$ J/g and $\Delta h_f(\beta) = 168.5$ J/g, respectively, was assumed for calculations [31].

2.3.2. WAXS

Computer controlled X-ray diffractometer equipped with a pole figure attachment, coupled to a sealed-tube source of filtered Cu Kα radiation, operating at 50 kV and 30 mA (Phillips) was used for X-ray measurements. The $\Theta-2\Theta$ scans were collected with the step of 0.05°. From the obtained diffractograms the phase composition, including content of β-phase, was estimated. For accurate determination of phase structure the peak separation procedure was applied. The program OptiFit [32,33] based on multi-criteria optimization algorithm was used for this purpose.

The texture of deformed samples was studied using the X-ray pole figure technique (for overview of this technique see Ref. [34]). The specimens in the form of slices approx. 2 mm thick were cut out from the deformed samples in the plane perpendicular to the flow direction (FD). Such an orientation of specimens benefited in reduction of the influence of analytical errors resulting from defocusing of the beam when the specimen was tilted during data collection. The (100), (110) and (111) crystal planes of trigonal β-form of iPP were analyzed (diffraction maxima centered around $2\Theta = 14.2°$, 16.1° and 21.1°, respectively) and the respective pole figures were constructed. For monoclinic α-crystals pole figures of (110) and (040) planes (reflections at $2\Theta = 14.1°$ and 16.9°, respectively) were measured. Additionally, the peak around 42.5° representing several planes of α- and β-crystal, all with normals oriented close to the direction of chain, as well as the intensity around $2\Theta = 15.0°$ correlated with the smectic phase, was analyzed. Experimental diffraction data were corrected for background scattering, sample absorption and defocusing of the beam. Obtained pole figures were plotted with the POD program (Los Alamos National Lab, NM). Other details of the experimental procedure were described elsewhere [21].

2.3.3. SAXS

Lamellar structure of raw and deformed samples was probed by 2-dimensional small angle X-ray scattering (2-D SAXS). The 1.1 m long Kiessig-type camera was equipped with a tapered capillary collimator (X-ray Optical Systems) combined with additional pinholes (300 μm in diameter) forming the beam, and an imaging plate as a detector (Fuji). The camera was coupled to an X-ray source (sealed-tube, fine point Cu Kα, Ni-filtered radiation, operating at 50 kV and 40 mA; Philips). Exposed imaging plates were read with Phosphor Imager SI scanner and ImageQuant software (Molecular Dynamics). Long periods (LP) in the direction of interest were determined from appropriate 1-dimensional sections of 2-D patterns. LP was calculated from the position of the maximum of background and Lorentz corrected curve using the Bragg's law.

2.3.4. SEM

Specimens for microscopic observations were prepared in a two-step procedure. First, an internal surface of interest was exposed by cutting with an ultramicrotome (Tesla BS 490A). Next, that exposed surface was etched (1–2 h at room temperature) with a mixture containing 0.7 wt./vol.% of $KMnO_4$, dissolved in a 5:4:1 vol./vol. mixture of 95% sulfuric acid, 85% phosphoric acid and distilled water, respectively, according to the procedure developed originally by Olley et al. [35]. To improve etching the mixture was placed in an ultrasonic bath running periodically for short time periods during the etching process. Etched, washed accordingly [35] and dried specimens were coated with fine gold layer by ion-sputtering (JEOL JFC-1200) and examined with a scanning electron microscope (JEOL JSM-5500LV) operating in high vacuum mode and accelerating voltage of 10 kV.

3. Results

3.1. Initial phase composition

Raw, undeformed samples of plain (α-rich) and nucleated (β-rich) iPPs were characterized with DSC, WAXS and SAXS. The overall crystallinity estimated from DSC melting data was $X_c = 54$ wt.% and 59 wt.% for α- and β-rich sample, respectively.

In β-nucleated sample the overlapping melting peaks characteristic for β- and α-modification were observed. A rough estimate of the phase composition (peaks separated simply by the vertical drop line drawn from the minimum between respective peaks to the baseline; contribution of each phase calculated with the values of heat of fusion appropriate for β- and α-phase) yielded the content of β-phase of approx. $X_\beta = 26$ wt.% and of α-phase of approx. $X_\alpha = 33$ wt.%, which gave the contribution of β-crystals $k_\beta = X_\beta/(X_\beta + X_\alpha) = 0.44$.

The crystallinity of the β-sample calculated from X-ray data was $X_c = 62.7$ wt.%. Using the peak separation procedure the phase composition consisting of $X_\beta = 57.7$ wt.% of β crystalline phase, $X_\alpha = 5.0$ wt.% of α and 37.3 wt.% of amorphous component was determined. No mesophase was detected in the undeformed sample. This led to an estimation of β contribution to the crystalline phase $K_\beta = 0.92$, much higher than $k_\beta = 0.44$ estimated from DSC. The parameter K_β can be calculated from the equation [36]:

$$K_\beta = \frac{I_{\beta(110)}}{I_{\beta(110)} + I_{\alpha(110)} + I_{\alpha(040)} + I_{\alpha(130)}}$$

where $I_{\alpha(110)}$, $I_{\alpha(040)}$ and $I_{\alpha(130)}$ are the integral intensities of the strongest peaks of α-form attributed to the (110), (040) and (130) planes of monoclinic cell, respectively, while $I_{\beta(110)}$ is the intensity of the strongest (110) diffraction peak of the trigonal β-form[1], located at $2\Theta = 16.2°$. This parameter is only an estimate of the actual phase composition, because only the highest diffraction peaks are taken into account. However, since the other experimental peaks either contain contribution from both modification or are much lower than those considered, an error of estimation of the phase composition using the parameter K_β is relatively low. This parameter is commonly used in the literature.

Diffraction-based determination of phase composition seems to be much more precise and trustworthy than that obtained from DSC data. The contribution of β-phase $K_\beta = 0.92$ obtained from X-ray was confirmed independently by examination of several low magnification SEM micrographs, which demonstrated about 90–93% of the sample cross-section occupied by β-spherulites.

Long period was estimated from SAXS measurements. The obtained values of long period were 12.6 nm and 16.4 nm for α- and β-rich sample, respectively. Since the difference in crystallinity is not large it can be inferred that lamellae of β-phase are reasonably thicker than those of α.

3.2. Stress–strain behavior

Typical true stress–true strain curves obtained for samples of α- and β-rich material deformed by plane-strain compression at room temperature are shown in Fig. 1. The arrows above the curve of β-iPP indicate the true strains reached by β-iPP specimens taken for further structural investigations. Codes of these specimens, used in this paper, along with applied and permanent strains (the strain left in the sample after 12 weeks of recovery at room temperature) are given in Table 1.

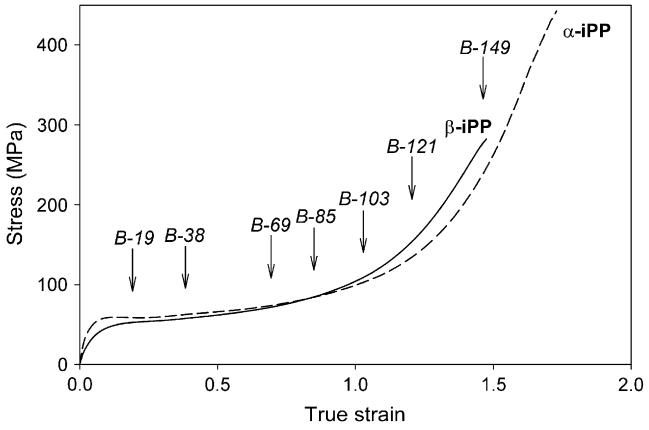

Fig. 1. Exemplary true stress–true strain curves of two samples of iPP rich in α- or β-crystal, compressed in a channel-die at room temperature with the constant true strain rate of 0.05 min^{-1}.

The true stress–true strain curves of α- and β-iPP show similar shape: no maximum near the yield point (i.e. no strain softening), short stage of low and moderate strains hardening followed by much stronger strain hardening prior to fracture. The determined curves are similar to the respective curves reported for α- and β-iPP deformed by uniaxial compression [26]. Similarly to uniaxial tension and compression β-iPP reveals lower elastic modulus and the stress at yield and initial stage of plastic flow as compared to α-iPP. The Young modulus of 1.13 GPa and 1.30 GPa and stress at yield (2% offset) of about 36 MPa and 50 MPa were found for β- and α-iPP sample, respectively. Samples of β-iPP demonstrate more intense strain hardening than α-iPP in the range of strain from 0.20 to 1.0 which results in intersection of their stress–strain curves at the true strain around $e = 0.85$. Karger-Kocsis [37] suggested that higher strain hardening in β-iPP can be attributed to the β → α phase transformation. Another, more convincing explanation offered by Xu et al. [26] is that β-crystals are less constrained since they do not have interlocking secondary lamellae ('cross-hatching' morphology characteristic for α-spherulites), which results in commencement of orientation

Table 1
Applied, permanent and recovered true strains of β-iPP specimens studied

Sample code	Applied true strain, e	Permanent plastic true strain, e_{pl}	Recovered strain, $e_r = e - e_{pl}$
B-19	0.19	0.06	0.13
B-38	0.38	0.20	0.18
B-69	0.69	0.49	0.20
B-85	0.85	0.64	0.21
B-103	1.03	0.81	0.22
B-121	1.21	0.97	0.24
B-149	1.49	1.21	0.28

[1] In this paper we use indexing of the crystal planes of β-crystals in accordance with the 3-chain trigonal unit cell: (100), (110) and (111) giving 3 strongest diffraction peaks observed at around $2\Theta = 14.2°$, 16.1° and 21.1°, respectively. The most common in the literature is the indexing consistent with the large 9-chain cell, leading to indices (210), (300) and (301) for the same crystalline peaks.

hardening of amorphous regions and crystallographic texturing at lower strains in β-rich sample than in α sample. The rate of strain hardening in the final deformation stage is similar for both the materials, yet this stage is primarily the property of the amorphous phase being now ultimately strained and oriented, while the original crystals are already heavily fragmented [38], which reduces constraints present at lower strains in α structure. Finally, fracture occurs in β-iPP earlier, at lower strain and stress than in α-iPP ($e_B = 1.5$ and $\sigma_B = 290$ MPa while 1.76 and 440 MPa for β- and α-iPP, respectively). While the deformation behavior of α- and β-iPP at low and moderate strain is similar to that reported for uniaxial compression [26] the ultimate properties are much different: ultimate strains observed in plane-strain compression are lower while the respective stresses are distinctly higher than in uniaxial compression, although the difference in the ultimate strain of α and β is preserved. This frequently observed difference between uniaxial- and plane-strain compression is explained by the presence of additional constraints imposed on the material when deformed in plane-strain conditions. These constraints lead to higher stress build-up.

Dimensions of deformed and then unloaded samples were measured over a period of time (up to 12 weeks) to determine the permanent plastic and recoverable strain components. It was found that all β samples demonstrated noticeable strain recovery, increasing slightly with an applied strain (cf. Table 1). This recovery was limited to the loading and flow directions, while the size along CD remained constant, as expected for plane-strain deformation. The recoverable strain component is attributed to the deformation and pseudo-elastic recovery of the amorphous component [38,39]. Highly deformed samples of α-iPP demonstrated similar strain recovery ($e_r = 0.34$ for $e = 1.76$) which indicates that the deformation of the amorphous component in highly strained β-iPP contributes to the deformation process similar to that in highly strained α-iPP samples.

3.3. Melting behavior

Fig. 2 presents DSC melting thermograms of β-iPP specimens deformed to the strains listed in Table 1. Undeformed α- and β-iPP are shown for reference. Specimens for DSC were cut out from the central part of the deformed samples in plane normal to CD in order to minimize the effect of shrinkage/expansion of the deformed specimen during heating on the measured heat flow.

The DSC curve of undeformed α-iPP exhibits a single melting peak at 164.2 °C, while the sample of undeformed β-iPP shows two peaks in the range 143.9–149.8 °C ascribed to melting of β-phase in addition to the peak representing melting of α-crystals at 164.1 °C. A double melting peak (β and β′) is observed for β-phase due to lamellae perfection and thickening within the β-phase [1,5,40]. Such behavior is observed usually in samples exhibiting large structural instability, crystallized at higher supercooling [5], similar to samples studied here, crystallized by fast cooling to 0 °C.

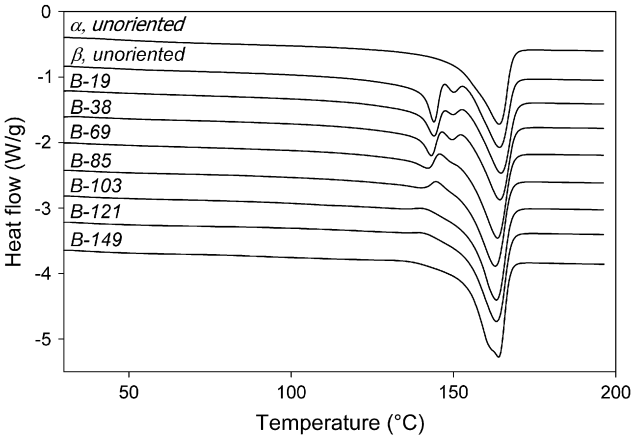

Fig. 2. Representative DSC thermograms of samples of raw α- and β-iPP and deformed samples of β-iPP. Curves were shifted along the heat flow axis for clarity of presentation.

The position of the melting peak of α-phase in the deformed β-iPP samples remains constant, near 164 °C, whereas peaks representing melting of β-phase shift slowly to lower temperatures with increasing strain (from 143.9 °C to 140.1 °C and from 149.8 °C to 148.4 °C for β and β′ peaks, respectively). Simultaneously both β and β′ peaks decrease gradually while that of the α-phase increases. Consequently, at strains above 0.4 the β′ peak disappears in the shoulder of α peak. The β peak can be recognized only to the true strain of $e = 1$ and then also dissolves in the expanding shoulder of the α peak. In any of the deformed samples no endotherm or exotherm related to the mesophase (which could be expected near 58 °C and 96 °C, respectively [41]) was observed. Such an evolution of the melting behavior with strain might suggest a continuous β → α transformation occurring upon deformation.

The overall heat of melting calculated from the thermograms in Fig. 2 decreases from 102.4 J/g to 98.4 J/g (ca. 4% reduction) suggesting slow decrease of overall crystallinity with increasing strain. From these data the contributions of β- and α-phase to overall crystallinity were estimated, as described in Section 3.1. Fig. 3 shows results of these rough estimations. The estimated initial overall crystallinity of the β-rich sample is 59 wt.%. It decreases with increasing the strain to 56 wt.% at $e = 1.49$. The estimated partial crystallinity of β-phase also decreases, yet much stronger, from $X_\beta =$ 26 wt.% in undeformed sample to approx. 10% in B-149 specimen ($e = 1.49$), while the partial crystallinity of α-crystals increases at the same time from $X_\alpha = 33$ wt.% to 46 wt.%. These results again suggest a continuous β → α transformation advancing with an increasing strain. As suggested by the reduction of overall crystallinity a small fraction of β-crystals is destroyed and transformed into amorphous phase. Similar changes of phase composition in β-rich iPP samples, inferred from DSC data, were reported for uniaxial compression [26] and uniaxial tension [31].

We must note, however, that an extreme caution is necessary in interpretation of these (or similar) results since, as already mentioned in Section 3.1, the phase composition

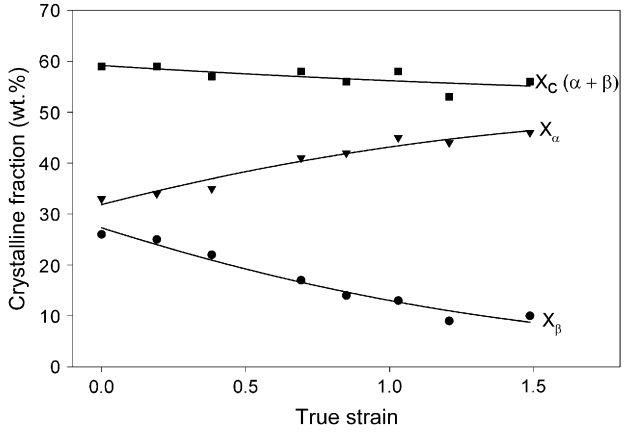

Fig. 3. The dependence of overall and partial crystallinities of α- and β-iPP on the true strain applied, derived from DSC data.

estimated for undeformed sample is very far from the X-ray based evaluation, supported by direct morphological observations, both giving the contribution of β-phase K_β above 0.9. Such a discrepancy is a result of large error of estimations based on melting data, which is caused by recrystallization of β-form to α-modification on heating. Additionally, kinetic of that recrystallization, hence the recorded heat flow depends on the heating rate applied. Thus, the DSC-estimated phase composition does not reflect at all the real phase composition of the material, while X-ray and morphology studies carried out at constant room temperature deliver undisturbed data. Comparison of $k_\beta = 0.44$ and $K_\beta = 0.92$ obtained for undeformed β-sample from DSC and X-ray, respectively, shows the magnitude of the error of the DSC-based estimation. For the same reason the DSC-based evaluation of phase composition in the deformed samples demonstrates similar low precision.

3.4. Evolution of phase composition upon deformation

Phase composition can be determined quite accurately from X-ray diffraction data. It is relatively easy for macroscopically isotropic samples of undeformed material. However, plastic deformation induces development of the crystalline texture. This results in an increase of intensity of crystalline diffraction peaks in particular directions, while suppression in others. As a result the area of any crystalline peak depends on the orientation of the sample with respect to the incident beam. Consequently, neither overall crystallinity nor contribution of the particular phase can be determined from a single diffraction pattern measured at any position of the sample in the diffractometer cradle. This is illustrated by Fig. 4a presenting diffraction patterns obtained for the same sample B-149 ($e = 1.49$) oriented in 3 orthogonal directions with respect to the incident beam. For every position of the specimen only planes of specific orientation (indicated in the plot) fulfill the Bragg's law and can give rise to the respective diffraction pattern. This example shows clearly that in order to determine the phase composition of a sample oriented by deformation it is necessary to measure diffraction patterns for all possible orientations of the

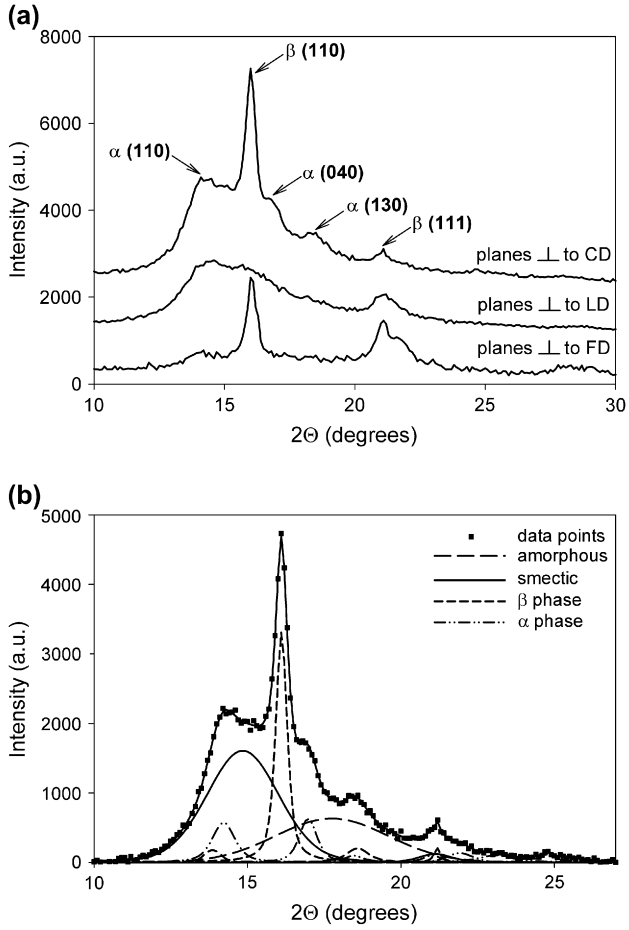

Fig. 4. Diffractograms of β-iPP sample B-149 subjected to the plane-strain compression to $e = 1.49$, collected at 3 orthogonal orientations of the sample with respect to the primary beam, probing planes of different orientation, as indicated (a), and an exemplary result of the peak separation applied to the same sample (b). In (a) the curves were shifted along the ordinate axis for clarity of presentation.

sample with respect to primary beam (procedure which is similar to data collection for pole figure), determine the phase composition from each diffractogram and then perform spatial averaging of these partial data. Since crystalline peaks of iPP overlap with each other and additionally with the amorphous halo underneath it is necessary to perform peak separation to every diffraction curve for accurate determination of the phase composition. That peak separation procedure, performed with the computer program 'OptiFit' [32,33]), is illustrated in Fig. 4b. Since both data collection and their evaluation, including peak separation, are time consuming we decided to reduce the number of collected and analyzed curves to 12 (for each specimen studied), obtained at the representative orientations of the specimen in the diffractometer cradle. These orientations were pre-selected on the basis of texture analysis (reported later, in Section 3.7). Such a limitation was a compromise between accuracy of the estimation and the time needed for measurements and calculations. Every specimen tested was positioned in the diffractometer cradle at the polar angle of $\rho = 0°$, 30°, 60° or 90° and the azimuth angle of $\varphi = 0°$, 45° or 90°.

Analysis of the collected diffraction data demonstrated that for some sample orientations diffraction curves exhibited a significant contribution of the smectic phase in addition to crystalline α and β and amorphous component, as illustrated in Fig. 4b. Therefore, for every curve evaluated the presence of all 4 phases had to be assumed in the initial set of fit parameters for peak separation. After peak separation the contribution of every phase to the diffraction curve was calculated from the areas of respective peaks. The obtained values were averaged spatially in order to get the phase composition of the sample. In this way the evolution of contributions of 2 crystalline (α and β) and 2 non-crystalline (smectic and amorphous) components to the phase composition was estimated for deformed samples in the strain range studied. Results are presented in Fig. 5.

In order to check the validity of performed estimations the sample of the highest strain, B-149 was ground into the fine powder. The sample was immersed in liquid nitrogen during this procedure to facilitate brittle fracture and minimize any unwanted plastic deformation on grinding. The collected powder was compacted gently to obtain a powder sample of a nearly random crystallite orientation (unfortunately, some fraction of grains demonstrated a flake- or needle-like shape, therefore tend to produce some crystal orientation on compaction). Next, the powder diffraction curve was determined for that sample, and its phase composition was estimated using the same peak separation procedure. The results are presented in Fig. 5 with open symbols. It can be seen that both methods of phase composition evaluation (i.e. spatial averaging and analysis of the powdered sample) led to quite similar results, which can confirm the validity of the used averaging approach. That approach was preferred in this study over the preparation of a powder sample since grinding of oriented samples appeared very difficult, required relatively large quantity of the material to be powdered and produced frequently grains of anisotropic shape, which could result in some unwanted anisotropy of the compacted powder sample, and consequently in an inaccurate estimation of the phase structure.

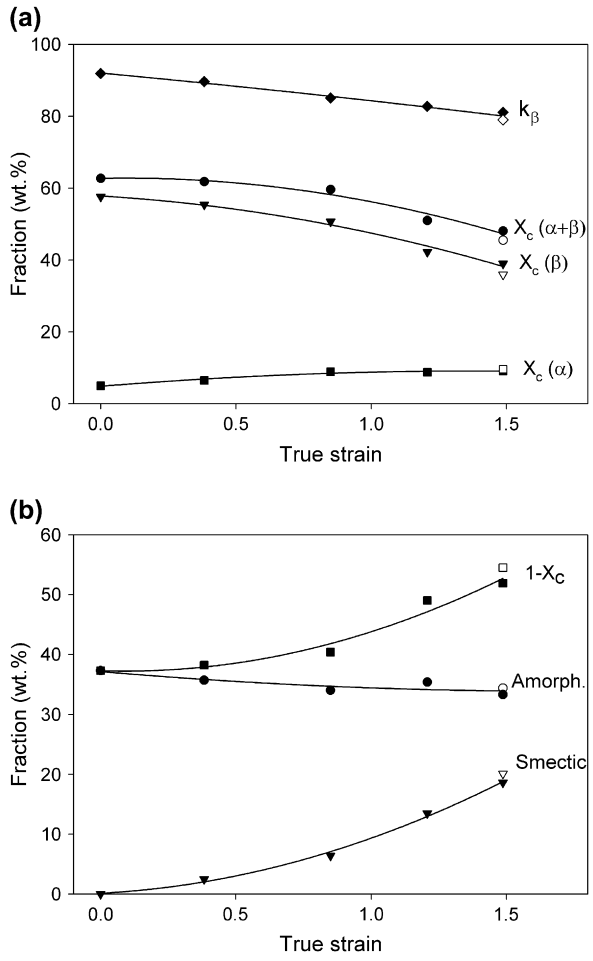

Fig. 5. The overall crystallinity, partial crystallinities of α- and β-phase and the contribution of the β-phase to the overall crystallinity (a) and the content of amorphous and smectic phases (b), plotted as a function of the true strain. Open symbols represent the results obtained for the powdered sample ($e = 1.49$).

Data presented in Fig. 5 demonstrate that the overall crystallinity, X_c, decreases from 63 wt.% to 48 wt.% when the applied true strain increases from $e = 0$ to 1.49. This decrease is stronger than that estimated from DSC (cf. Fig. 3). Moreover, the contributions of α and β crystal phases to the overall crystallinity are quite different than those evaluated from DSC: the content of β-phase X_β decreases from 58 wt.% to 39 wt.% (reduction by 19%), while the content of α-crystals X_α increases only by 4 wt.%, from the initial value of 5 wt.% to 9 wt.% at $e = 1.49$. It indicates that, in contrast to DSC results, only a part of β-phase is replaced by α-phase during deformation. The remaining part of destroyed β-crystals is transformed rather to the smectic phase, contribution of which increases from 0% to nearly 19%. At the same time the amount of amorphous component decreases from approx. 37 wt.% to 33 wt.%, i.e. by 4 wt.%. Comparison of the above numbers indicates that the smectic phase is created probably during deformation process from both transformed β-form crystals and at least partially from the amorphous component becoming increasingly oriented with advancing strain. That evolution of the phase structure of the β-iPP with strain suggests that in deformation at room temperature the β → smectic phase transformation is much more intense than β → α transformation, postulated frequently to be the primary deformation mechanism of β-crystals at both room temperature and elevated temperatures [22–24,26].

It is also worth to note that the most intense scattering of the smectic phase in deformed samples is observed along CD direction, which indicates a strong orientation of the smectic phase created during deformation process. The observed variation in scattering intensity is consistent with the preferred orientation of the direction of chain within smectic domains along the flow direction, FD. The orientation of the smectic component is discussed later in this section.

We believe that the phase composition and its evolution, determined from the diffraction data and discussed above are more precise and reliable estimation of the composition than the estimation based on the melting data since the X-ray based evaluation was done at the temperature of deformation,

without heating the samples up to the recrystallization point, which was the case of DSC measurements.

3.5. Morphological alterations

In order to reveal the evolution of morphology of β-iPP during plane-strain compression scanning electron microscopic (SEM) observations were performed. Fig. 6 shows representative micrographs obtained for samples of deformed β-iPP. All investigated specimens were cut out in the FD–LD plane, i.e. viewed along CD, with FD direction set vertically.

Examination of micrographs reveals that undeformed β-iPP shows a clear spherulitic morphology. The holes left by the particles of nucleant can be frequently observed in centers of β-spherulites. Another feature of the observed structure is that spherulites of β-modification do not show the 'cross-hatched' lamellar morphology, characteristic for the α-phase [1–4]. The lamellae in β-spherulites are almost straight, growing radially from spherulite centers. Micrographs of deformed samples demonstrate that fine deformation bands develop shortly beyond the yield point. First bands can be observed already in the sample B-19 ($e = 0.19$, $e_p = 0.06$; cf. Fig. 6b). These bands are probably initiated by the interlamellar slide, i.e. the shear of amorphous layers although some bands crossing the lamellae transversely can also be observed. These transverse bands indicate the localized deformation by crystallographic mechanisms. At later stages of deformation such lamellae undergo local destruction and fragmentation by developing deformation bands. Another mechanism which can be identified already in this sample of low strain is the cooperative kinking of lamella, initially limited to those lamellae which were oriented with their normals perpendicular to the load direction (small kink band inside a single spherulite indicated with an arrow in Fig. 6b, the more advanced lamellar kinks are clearly seen on the right-hand side of Fig. 6d). With increasing strain the number of shear bands increases substantially, which leads to the formation of a dense array of crossing deformation bands in the sample (cf. Fig. 6c–f). Simultaneously, these bands, oriented initially approx. 45° with respect to LD or FD rotate gradually towards FD. Finally,

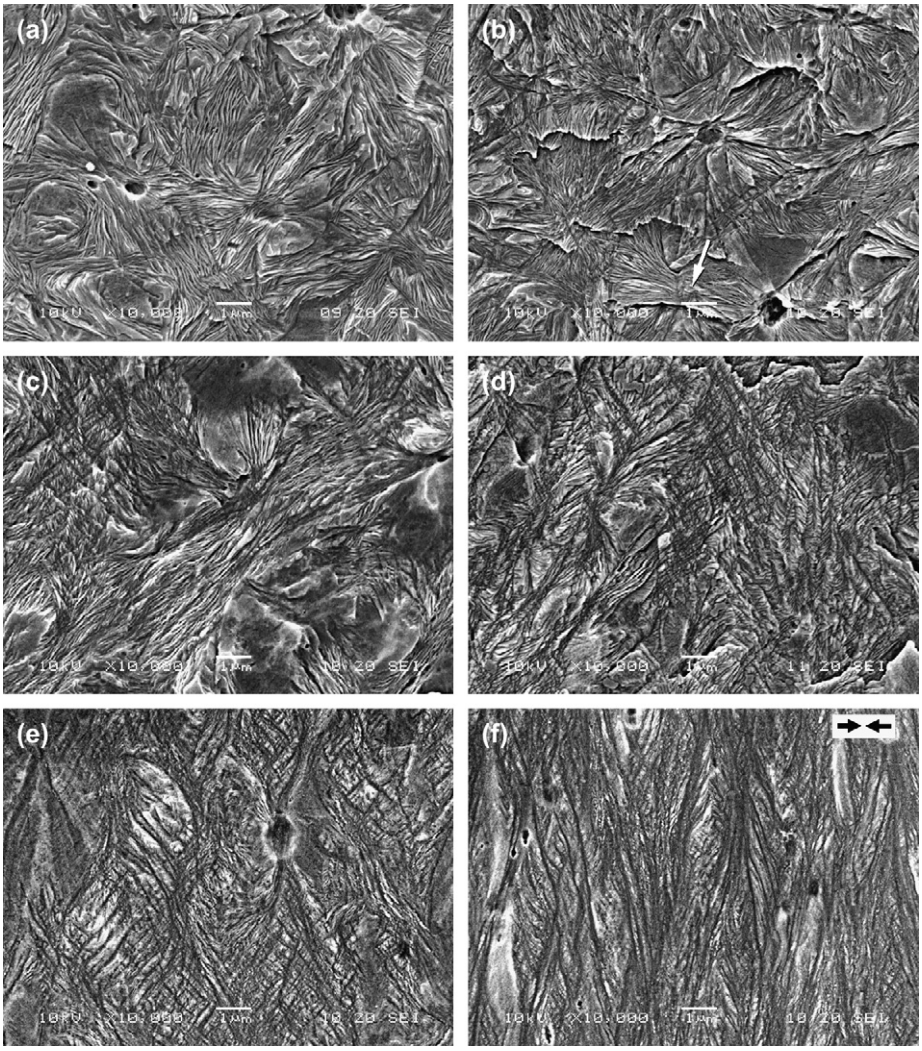

Fig. 6. Scanning electron micrograph of raw (a) and compressed β-iPP samples: (b) B-19, (c) B-38, (d) B-69, (e) B-85, (f) B-121. All specimens were cut along the LD–FD plane and etched. The direction of the compressive load, the same for all micrographs, is marked in (f). The 1 μm scale bar is shown on each micrograph.

Table 2
The average angle between shear bands (S.B.) and FD, determined from SEM micrographs and the angle between lamella normals (n) and LD determined from 2-D SAXS patterns of deformed samples

Sample	B-19	B-38	B-69	B-85	B-103	B-121	B-149
True strain	0.19	0.38	0.69	0.85	1.03	1.21	1.49
∠ (S.B., FD)	~50	47	35	30	23	20	18
∠ (n, LD)		47	28	26	25	22	20

at the true strain of 1.49 the angle between shear bands and FD decreases to approx. 18°. In Table 2 the average angle between deformation bands and FD determined from SEM micrographs is presented along with the angle between lamellar normals and LD (equivalent to the angle between lamellar surfaces and FD) derived from SAXS. Multiplication of deformation bands, their rotation as well as lamellar kinking between bands results in destruction of the spherulitic structure above true strain of $e = 0.85$ (in the sample B-85, shown in Fig. 6e, some heavily deformed remnants of the original spherulitic structure can be still recognized, while the spherulitic structure is lost completely in samples of higher strain, as B-121 presented in Fig. 6f). The final morphology developed in the sample B-149 deformed to the strain of $e = 1.49$ is similar to that observed in B-121. It consists of a dense array of crossing deformation bands heavily tilted towards FD. Between these bands the short lamella fragments are also highly tilted or arranged in a chevron pattern, produced by cooperative kinking and associated rotations of lamellae. Apparently, that kinking initially limited to only those lamellae oriented with their normals along FD, extended at later stages of deformation also to other lamellar stacks deviating from the 'ideal' orientation parallel to FD. Development of similar kinks was observed in β-iPP deformed in simple shear [42] and in tension [43]. Formation of a chevron morphology produced by kinks was studied recently in detail by Krumova et al. [43].

3.6. Evolution of lamellar structure

Fig. 7 illustrates the evolution of lamellar structure of the β-iPP. Samples were probed with 2-D SAXS in the FD–LD projection (primary beam along CD) and the FD–CD projection (LD-view). All 2-D SAXS patterns were collected after complete recovery of deformed samples (at least 2 months at room temperature). The FD–LD patterns demonstrate the evolution of the shape from a circle to an ellipse at the true strain increasing from 0 to below 0.38, which can suggest the deformation by simultaneous crystallographic slip mechanisms and interlamellar shear. Around true strain of $e = 0.38$ the 4-point signature begins to emerge in CD-view pattern, while in LD-view an ellipse is flatten out and replaced by two arcs oriented along FD direction. In both patterns the scattering along FD fades away, which leads to a disappearance of long period along FD at higher true strains. The described features develop further with increasing strain. The 4-point signature in CD-view patterns strengthens with advancing strain, which indicates the formation of two populations of lamellae, both oriented with their normals in the FD–LD plane, symmetrically

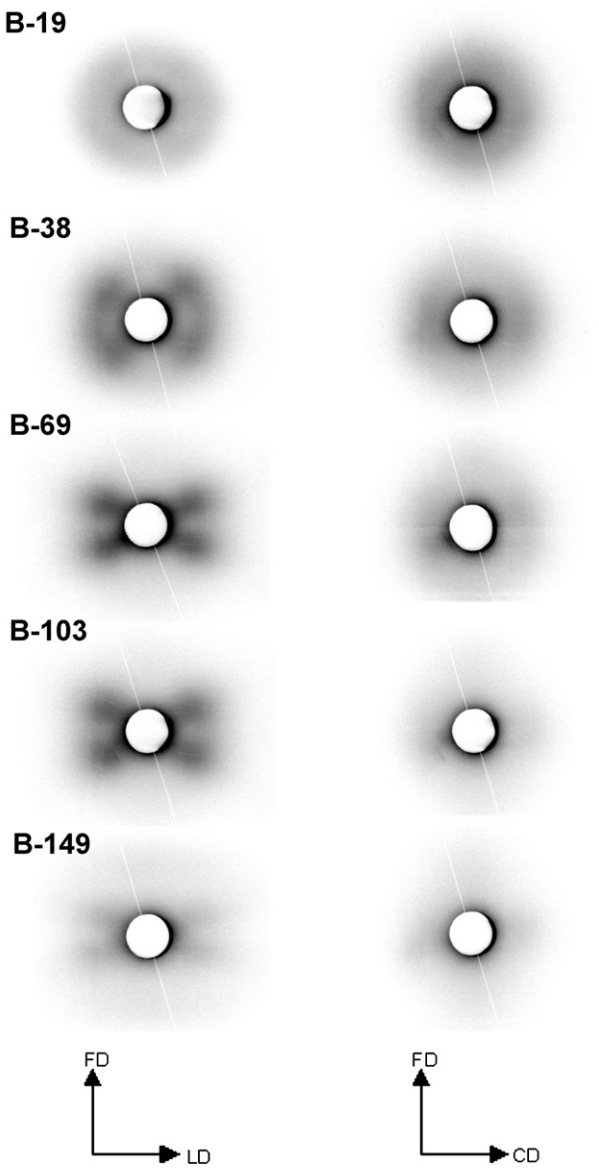

Fig. 7. 2-D SAXS patterns obtained for a series of β-iPP samples, deformed in the plane-strain compression. Left-side column: CD-view, right-side column: LD-view. Sample codes indicate the true strain applied (cf. Table 1).

at some acute angle with respect to FD. The intensity of scattering maxima in CD-view is considerably higher than those observed in LD-view patterns. This suggests that these two populations described above are the dominant ones in the entire domain of lamellar orientation. The angle between normals of these lamellae and LD decreases with increasing strain (cf. Table 2), which demonstrates their continuous rotation towards FD upon advancing deformation. As demonstrated in Table 2 this angle correlates well with the orientation of shear bands which demonstrates an influence of these bands on orientation of lamellae, which was already suggested by SEM observations.

Another, new feature can be recognized in CD-view pattern of the sample B-149. This is a set of two relatively weak horizontal stripes located in the direction of flow. At the same time the 4-point component shows weaker scattering

as compared to patterns for lower strains. Such features of scattering pattern were found to be associated with heavily fragmented lamellae, where all crystalline fragments are progressively oriented with their normals along FD, yet still arranged in a chevron-like pattern [29,44]. Such an arrangement was found to develop in deformed polyethylene due to heavy fragmentation of already kinked lamellae, related to advancing crystallographic slip within crystals and additionally due to an exhaustion and 'lock' of deformation of adjacent amorphous chains, now stretched nearly to the limit. This ultimate stretch results in a rapid increase of the stress, which triggers soon the fragmentation of lamella already thinned by crystallographic slip [29,41,44]. Fragmentation relieves partially constraints which in turn allow for more rotation of crystallites with the normal n towards FD and finally the formation of a new period along FD [29].

Long period (LP) determined from 2-D SAXS patterns in Fig. 7 for lamellae populations of different orientations generally decreases with an increasing true strain. That decrease is relatively slow (from LP = 16.3 nm at $e = 0$ to LP = 15.7 nm at $e = 1.49$) for LP determined along CD (LD-view patterns). The LP of lamellae oriented with normals around LD decreases slightly faster than that along CD. Similar slow decrease (down to 15.1 nm at $e = 1.49$) was observed for dominating lamellae giving rise to the 4-point pattern in CD-view. The continuously decreasing long period is a mark of crystallographic chain slip which results in thinning of lamellae. A very different behavior was found for the long period observed along FD, which shows a discontinuity: the initial LP = 16.3 nm disappears completely above $e = 0.39$. The new long period appears in this direction again in later stages of deformation, at $e > 1$, yet with a much lower value of 11 nm. This change is consistent with the hypothesis of heavy lamellae fragmentation and rotation as outlined above. Similar behavior was documented earlier for PE [29,44].

3.7. Evolution of crystalline texture

Fig. 8 presents a set of representative pole figures of two main crystallographic planes of β trigonal iPP crystals, (110) and (111), determined for deformed β-rich samples. Pole figures determined for other strains, although not presented here, are consistent with the set shown in Fig. 8. All presented figures were normalized, so that intensity of 1.0 is equivalent to the intensity expected for a randomly oriented sample. The scale of plots was chosen in such a way that white denotes concentration of poles lower than that of random distribution ($I < 1.0$), while gray shades and black show the concentrations of poles above it ($I > 1.0$). Pole figures of other crystal planes, e.g. $(100)_\beta$, $(110)_\alpha$ or $(040)_\alpha$ were also measured in this study. However, due to an overlapping of diffraction peaks all these figures were substantially influenced by the tails of very strong $(110)_\beta$ peak, which made these figures useless for texture analysis.

Another crystalline reflection analyzed by means of pole figures was the peak located around $2\Theta = 42.5°$. This peak is a complex one and includes contributions of several planes

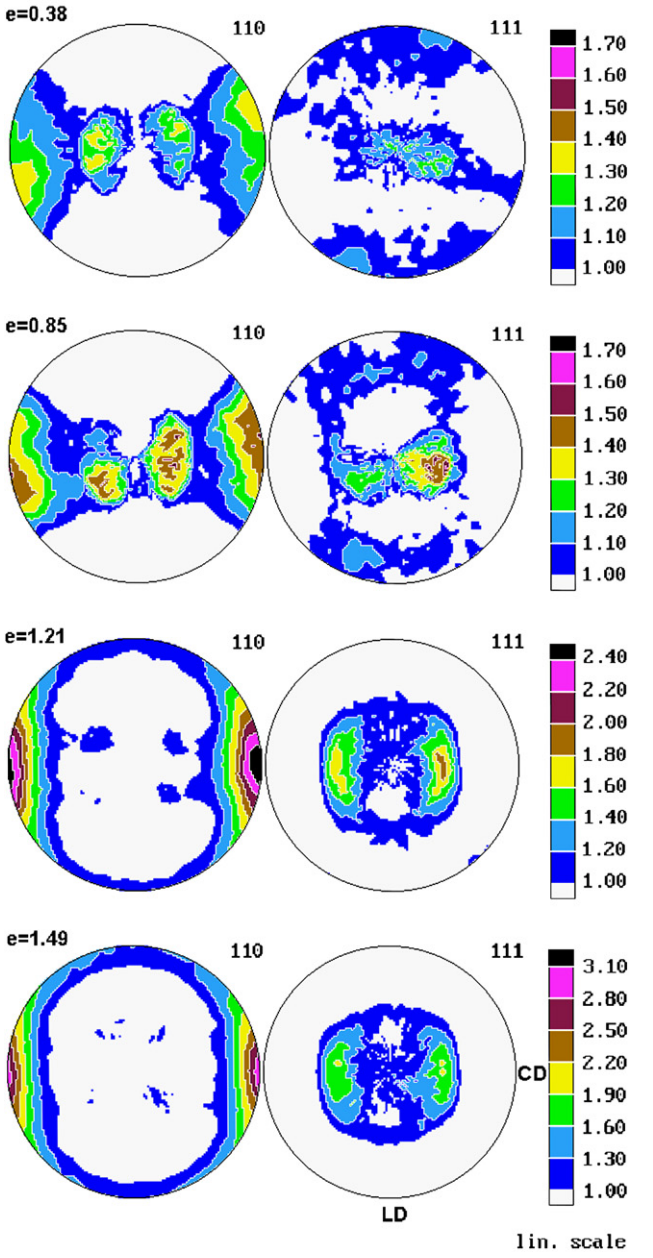

Fig. 8. Pole figures of the crystallographic planes (110) and (111) of trigonal β-iPP deformed in plane-strain compression to the true strain indicated.

of both β- and α-modification. One can expect in this peak a contribution of $(103)_\beta$ plane (at $2\Theta = 42.8°$; due to the hexagonal symmetry this plane is equivalent to $(013)_\beta$, $(1\bar{1}3)_\beta$, $(\bar{1}13)_\beta$, $(\bar{1}03)_\beta$ and $(0\bar{1}3)_\beta$), perhaps $(003)_\beta$ plane ($2\Theta = 41.8°$) as well as $(\bar{1}13)_\alpha$ and $(013)_{\alpha 2}$ planes ($2\Theta = 42.5°$). The diffraction peak at 42.5° is the best possible experimental measure of the molecular axis (c) in both crystalline phases of iPP since all contributing planes are nearly normal to the direction of chain in respective crystals (normal of $(103)_\beta$ makes an angle 12.8° with the chain axis, $(003)_\beta$ makes 0°, and $(\bar{1}13)_\alpha$ is only 5.8° away from the chain axis). Pole figures constructed for this composed peak are presented in Fig. 9. It shows that the orientation of chain axis in crystals starts to develop at the true strain of 0.19. Low concentration

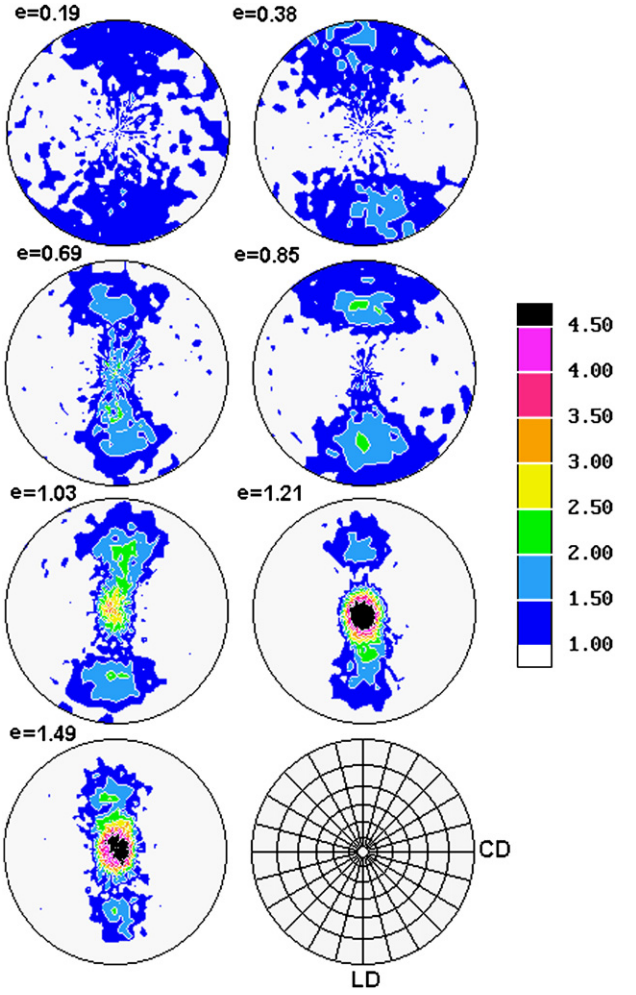

Fig. 9. Pole figures constructed for the composed peak at $2\Theta = 42.5^\circ$ for samples of various strain. The last plot shows the 15° net of stereographic projection.

of poles observed initially near LD ($e = 0.19-0.38$) form soon two clear maxima approximately 75° away from FD towards LD ($e = 0.69$). These maxima move gradually towards LD with increasing strain (to about 50° away from LD at $e = 1.49$). Such rotation towards LD of the chain axis suggests the activity of the crystallographic slip along the chain as a deformation micromechanism (note that lamella normals rotated in the opposite direction which is a clear indication of chain slip).

The intensity of the discussed maxima increases with strain increasing up to $e = 1.21$ and then reverses, i.e. decreases slightly with further advance of the strain. Concurrently (above $e = 0.86$), a new maximum develops right in the center of pole figure, indicating a rapidly growing population of crystals with chains oriented along FD. At $e = 1.21-1.49$ this orientation along FD becomes a dominating component of the molecular axis orientation distribution. Simultaneous change of the intensity of the two texture components in opposite directions implies that the new component oriented along FD is created from crystals oriented already 50–60° away from LD. Such a 'flip' of molecular axis cannot be a result of crystallographic slip which produces rather progressive reorientation. It cannot be also produced by shear bands and related rotations of lamellae, since these should rotate the *c* axis together with the lamellar normal in the opposite direction, i.e. away from LD. It can be, however, and most probably is, a result of kinking and subsequent severe fragmentation of lamellae, followed by their rotation which develops at high strains, as indicated by SEM and SAXS. Alternatively, this orientation can result from the newly created α-crystals by the β → α transformation. These crystals are generated most probably within shear bands, thus they should exhibit the orientation of their molecular axis close to LD. However, such α-crystals are produced in a rather small quantity (only 4 wt.%, cf. Fig. 5), probably too low to give such a strong texture component as observed experimentally. Secondly, if this was the case one should observe a gradual development of this texture component already at low strains since deformation bands, and therefore oriented α-crystals were formed from the beginning of plastic deformation process.

The above reported evolution of orientation of molecular axis in crystals is accompanied by the changes of orientation of poles of $(110)_\beta$ and $(111)_\beta$ planes, illustrated in Fig. 8. At the true strain below 1.0 the (110) normals are grouped in maxima distributed along two great circles oriented perpendicular to chain direction, as seen from Fig. 9. Number and positions of maxima along these great circles reflect the hexagonal symmetry of the β structure. Pole figures of (111) planes seem to agree with both chain and (110) plane orientations. At strains above $e = 1$, along with the discussed primary chain orientation developing along FD, the poles near the center of (110) pole figure dissolve. That figure becomes to be dominated by two maxima located near CD, both sharpening with the increasing strain. The lack of other maxima, which could be expected now along the equatorial circle, is probably related to an error produced by the scattering from the smectic phase, strongly modifying the intensities measured along this circle and causing an apparent enhancement of the intensity along CD (see diffraction curves presented in Fig. 4). This can lead to an artificial rise of the pole distribution along CD while relative reduction of it in other positions along the equator.

Poles in the (111) figure rotate simultaneously with poles of (110) to the positions on the circle approx. 50° away from FD, with two well developed maxima ca. 50° away from LD towards CD, which is quite consistent with other pole figures determined for the respective strain ($e = 1.21-1.49$).

Since X-ray phase analysis revealed the formation of the smectic phase in relatively large quantities we attempted to use pole figures technique to find its preferred orientation developing upon deformation. In order to do so, the pole figures were constructed from experimental intensities collected at the diffraction angle $2\Theta = 15^\circ$, i.e. the angle at which the maximum of the first smectic peak is located. Of course, without separation of the contribution of amorphous component and tails of crystalline reflections of $(110)_\alpha$, $(100)_\beta$ and $(110)_\beta$ such figure is merely a crude approximation of the orientation distribution of the smectic phase. Nevertheless, it can still provide some useful information. Fig. 10 presents the results of this approach applied to two samples, deformed to the true

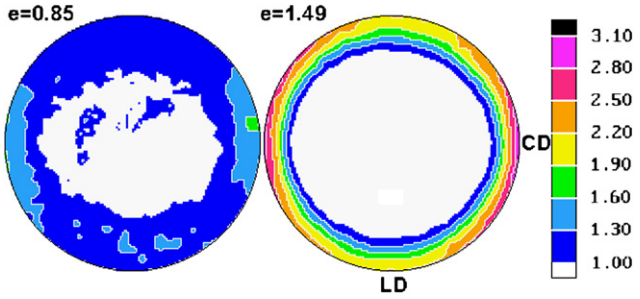

Fig. 10. Pole figures constructed from the experimental intensities measured at $2\Theta = 15°$, illustrating the orientation of (100) pseudo-planes in the smectic phase in samples B-85 ($e = 0.85$) and B-149 ($e = 1.49$).

strain of $e = 0.85$ and $e = 1.49$, respectively. Both pole figures demonstrate the same feature: a clear orientation of smectic (100) pseudo-planes giving rise to the maximum of distribution observed near CD, indicating the preferred orientation of chains in the smectic domains along the direction of flow, FD. The distribution of poles is sharper and stronger in sample B-149 ($e = 1.49$) than B-85 ($e = 0.85$). On the other hand, practically no rotation of the preferred orientation along CD with increasing strain can be observed. Such a 'texture' and its evolution are consistent with the molecular chain orientation around FD, which can be expected for the mesophase created by the β → smectic phase transformation proceeding within deformation bands.

4. Discussion

Results presented in the previous section allow to summarize the deformation behavior of β-iPP in the following sequence: above the elasticity limit the plastic deformation starts with the deformation of the amorphous layers by their shear (interlamellar slip) and deformation of lamellar crystals by crystallographic chain slip, which is most probably the (110)[001] slip, suggested earlier by Asano et al. [27]. Due to hexagonal symmetry of the β structure this (110)[001] slip is equivalent to two other chain slip systems $(1\bar{2}0)[001]$ and $(2\bar{1}0)[001]$ which can operate in planes $(1\bar{2}0)$ and $(2\bar{1}0)$, equivalent to (110). Slip in other planes, e.g. (100) is also probable. Initiation of plastic deformation by these two mechanisms is relatively easy in β-iPP as compared to α-iPP since β-crystals do not have interlocking secondary lamellae, therefore are less constrained from deformation than interlocked crystals of α-form ('cross-hatching' morphology characteristic for α-spherulites). This makes both interlamellar shear and crystallographic slip easier than in α-iPP [21,26,45]. For the same reason orientation hardening of amorphous regions and crystallographic texturing commences at lower strains in β-rich sample than in α sample which results in higher initial rate of the strain hardening of β samples at low and moderate strains, below $e = 0.85$ [26].

Interlamellar shear of amorphous layers develops relatively easily along nearly straight and long β-lamellae, which gives rise to localization of deformation in thin deformation bands. These bands develop initially around 45° with respect to loading direction due to the highest resolved shear stress at this orientation. As demonstrated by SEM micrographs fine shear bands, when propagating across the sample, encounter also lamellae oriented perpendicularly to the band. Apparently, the band can propagate across those lamellae utilizing crystallographic slip localized in the zone of the thickness of the band. The slip system operating there can be either (110)[001] chain slip or any transverse slip, e.g. $(110)[1\bar{1}0]$, $(1\bar{2}0)[210]$ [26], or any other allowed slip system.

An intense, yet highly localized deformation of crystals within deformation bands leads soon to a local destruction of lamellae and consequently their fragmentation [29]. The destroyed part is transformed either into smectic phase or into new α crystal. At room temperature, however, the primary transformation is rather the β → smectic phase transformation, while β → α transformation seems to be a secondary one. Similar observations were reported in the past for tensile deformation of β-rich iPP at room temperature [22,25,46]. The β → smectic transformation brings the material locally to the less ordered and less stable state, yet exhibiting higher chain mobility, which allows for easier (less energy consuming) pathway of plastic deformation [47]. Apparently, room temperature is not high enough to allow for local chain rearrangements resulting in the formation of the stable α-form (β → α). However, it was postulated that with an increase of the temperature of deformation relative weights of these two transformations change [22,25], especially at deformation temperatures above 80 °C, where smectic phase is known to turn into stable α-crystals [47,48]. This problem is addressed in our current investigation. Both β → smectic and β → α phase transformations are the solid-to-solid transformations – there is no indication of any melting and recrystallization process. In addition to the above discussed transformations, about 4% of amorphous phase is transformed to more ordered state, likely smectic. This ordering results probably from high molecular orientation of amorphous chains within heavily sheared amorphous interlamellar layers at high local strain.

The β → α solid state phase transformation requires reversal of the helical handedness. The mechanism of this was explained by Xu et al. [26] as a simultaneous solid transformation that consists of a process of transverse partial slip along (110) or (120) plane of β crystal lattice and a shear of that lattice, all in the presence of conformational defects. The propagation of these conformational defects along chains provides the reversal of helical handedness required by the β → α transformation.

In addition to homogeneous crystallographic slip processes and the deformation mechanism localized in deformation bands another deformation mechanism is activated at relatively low strains. This is the cooperative kinking of lamellae, initially limited to the lamellae oriented normally with respect to LD and becoming more widespread in lamellae already partially fragmented by fine deformation bands. That kinking and related rotations of lamellae offer additional route of fast orientation of molecular axis towards the flow direction FD and together with the action of deformation bands produce a chevron-like lamellar morphology.

At large strains, well above $e = 1$, advanced slip processes and high stretch of amorphous material in sheared interlamellar layers bring further fragmentation of lamellar crystals followed by a fast rotation of resulting unconstrained small crystallites with their chain axis towards FD. This process leads to the formation of the final texture of highly deformed β-iPP material with molecular axis of both crystalline and smectic phases oriented along the direction of flow.

5. Conclusions

Plane-strain compression experiments, reported in this study, allowed to find out the deformation sequence in β-iPP and the engaged deformation mechanisms. The most important were interlamellar slip operating in the amorphous layers and resulting in localization of deformation in numerous fine deformation bands and the crystallographic slip systems, including the (110)[001] chain slip and (110)[1$\bar{1}$0] transverse slip.

Advanced deformation within deformation bands leads to β → smectic and β → α solid state phase transformations. At room temperature the β → smectic transformation is the primary transformation, yielding the oriented smectic phase with the relatively high concentration of 19 wt.% at the true strain of $e = 1.49$. As a result of the deformation-induced phase transformation within numerous fine deformation bands the β-lamellae are locally destroyed and fragmented into smaller crystals.

Another deformation mechanism is the cooperative kinking of lamellae, leading to their reorientation and together with the action of deformation bands producing a chevron-like lamellar arrangement. At high strains, above $e = 1$, an advanced crystallographic slip and high stretch of amorphous material due to interlamellar shear bring further heavy fragmentation of lamellar crystals partially fragmented earlier by deformation bands. This fragmentation is followed by fast rotation of small unconstrained crystallites with chain axis towards FD. This process leads to the development of the final texture of the highly deformed β-iPP with molecular axis of both crystalline and smectic phases oriented along the direction of flow.

Acknowledgement

This work was financed in part from the budget sources for science in the years 2005–2008 as a research project (grants 3 T08E007 28 and 3 T08E008 30).

References

[1] Karger-Kocsis J, editor. Polypropylene structure, blends and composites. London: Chapman and Hall; 1995.
[2] Norton DR, Keller A. Polymer 1985;26:704–16.
[3] Yamada K, Matsumoto S, Tagashira K, Hikosaka M. Polymer 1998;39:5327–33.
[4] Keith HD, Padden FJ, Walter NM, Wyckoff HW. J Appl Phys 1959;30:1485–8.
[5] Varga J. J Macromol Sci 2002;B41:1121–71.
[6] Garbarczyk J. Polymer 1981;22:562–4.
[7] Jacoby P, Bersted BH, Kissel WJ, Smith CE. J Polym Sci Polym Phys Ed 1986;24:461–91.
[8] Varga J, Mudra I, Ehrenstein GW. J Appl Polym Sci 1999;74:2357–68.
[9] Li X, Hu K, Ji M, Huang Y, Zhou G. J Appl Polym Sci 2002;86:633–8.
[10] Chen HB, Karger-Kocsis J, Wu JS, Varga J. Polymer 2002;43:6505–14.
[11] Varga J, Karger-Kocsis J. J Polym Sci Polym Phys Ed 1996;34:657–70.
[12] Wu CM, Chen M, Karger-Kocsis J. Polymer 1999;40:4195–203.
[13] Somani RH, Hsiao BS, Nogales A, Srinivas S, Tsou AH, Sics I, et al. Macromolecules 2000;33:9385–94.
[14] Lovinger AJ, Chua JO, Grythe CC. J Polym Sci Polym Phys Ed 1977;15:641–56.
[15] Meille SV, Ferro DR, Brückner S, Lovinger AJ, Padden FJ. Macromolecules 1994;27:2615–22.
[16] Lotz B, Kopp S, Dorset D. CR Acad Sci Ser II Paris 1994;319:187–92.
[17] Kotek J, Kelnar I, Baldrian J, Raab M. Eur Polym J 2004;40:679–84.
[18] Raab M, Scudla J, Kolarik J. Eur Polym J 2004;40:1317–23.
[19] Osawa S, Porter RS, Ito M. Polymer 1994;35:551–7.
[20] Hirsch JR, Wang PT. Texture Microstruct 1991;13:101–22.
[21] Pluta M, Bartczak Z, Galeski A. Polymer 2000;41:2271–88.
[22] Chu F, Yamaoka T, Kimura Y. Polymer 1995;36:2523–30.
[23] Li JX, Cheung WL. Polymer 1998;39:6935–40.
[24] Karger-Kocsis J, Varga J. J Appl Polym Sci 1996;62:291–300.
[25] Shi G, Chu F, Zhou G, Han Z. Macromol Chem 1989;190:907–13.
[26] Xu W, Martin DC, Arruda EM. Polymer 2005;46:455–70.
[27] Asano T, Fujiwara Y. Polymer 1978;19:99–108.
[28] Lezak E, Bartczak Z. Fibres Text Eastern Eur 2005;13(53):51–6.
[29] Galeski A, Bartczak Z, Argon AS, Cohen RE. Macromolecules 1992;25:5705–18.
[30] Young RJ, Bowden PB, Ritchie JM, Rider JG. J Mater Sci 1973;8:23–36.
[31] Li JX, Cheung WL, Demin J. Polymer 1999;40:1219–22.
[32] Rabiej M. Polimery 2002;47(6):423–7.
[33] Rabiej M. Polimery 2003;48(4):288–95.
[34] Alexander LE. X-ray diffraction methods in polymer science. New York: Wiley-Interscience; 1969.
[35] Olley RH, Hodge AM, Bassett DC. J Polym Sci Polym Phys Ed 1979;17:627–43.
[36] Turner-Jones A, Aizlewood JM, Beckett DR. Macromol Chem 1964;75:134–58.
[37] Karger-Kocsis J. Polym Eng Sci 1996;36:203–10.
[38] Bartczak Z, Kozanecki M. Polymer 2005;46:8210–21.
[39] Bartczak Z. Polymer 2005;46:10339–54.
[40] Juhasz P, Varga J, Belina K, Belina G. J Macromol Sci Phys 2002;B41:1173–89.
[41] Wang ZG, Hsiao BS, Srinivas S, Brown GM, Tsou AH, Cheng SZD, et al. Polymer 2001;42:7561–6.
[42] Castelein G, Coulon G, G'Sell C. Polym Eng Sci 1997;37:1694–701.
[43] Krumova M, Hennig S, Michler GH. Philos Mag 2006;86:1689–712.
[44] Bartczak Z, Lezak E. Polymer 2005;46:6050–63.
[45] Aboulfaraj M, G'Sell C, Ulrich B, Dahoun A. Polymer 1995;36:731–42.
[46] Riekel C, Karger-Kocsis J. Polym Commun 1996;40:541–5.
[47] Seguela R. J Macromol Sci Part C Polym Rev 2005;45:263–87.
[48] Seguela R, Staniek E, Escaig B, Fillon B. J Appl Polym Sci 1999;71:1873–85.